

NEUROSCIENCE

In vivo direct imaging of neuronal activity at high temporospatial resolution

Phan Tan Toi^{1,2,†}, Hyun Jae Jang^{3,4,†}, Kyeongseon Min⁵, Sung-Phil Kim⁶, Seung-Kyun Lee^{1,2,†}, Jongho Lee⁵, Jeehyun Kwag^{3,7,*}, Jang-Yeon Park^{1,2,*}

There has been a long-standing demand for noninvasive neuroimaging methods that can detect neuronal activity at both high temporal and high spatial resolution. We present a two-dimensional fast line-scan approach that enables direct imaging of neuronal activity with millisecond precision while retaining the high spatial resolution of magnetic resonance imaging (MRI). This approach was demonstrated through in vivo mouse brain imaging at 9.4 tesla during electrical whisker-pad stimulation. In vivo spike recording and optogenetics confirmed the high correlation of the observed MRI signal with neural activity. It also captured the sequential and laminar-specific propagation of neuronal activity along the thalamocortical pathway. This high-resolution, direct imaging of neuronal activity will open up new avenues in brain science by providing a deeper understanding of the brain's functional organization, including the temporospatial dynamics of neural networks.

Advanced noninvasive neuroimaging methods provide valuable information on the brain's functional organization, but they have obvious pros and cons in terms of temporal and spatial resolution. Functional magnetic resonance imaging (fMRI) using the blood oxygenation level-dependent (BOLD) effect provides spatial resolution on the order of millimeters. However, its temporal resolution is limited by slow hemodynamic responses to neuronal activities such as spikes (1), whereas recent advances have been made in imaging subsecond oscillatory neuronal dynamics (2). Because there is no direct correspondence between BOLD signals and spiking activity (3–5), BOLD-fMRI provides indirect information about neuronal activity, intrinsically limiting the spatial and temporal precision (5, 6). By contrast, electroencephalography (EEG) and magnetoencephalography (MEG) provide excellent temporal resolution in the millisecond range, but spatial information is limited to centimeter scales (7). Thus, while harnessing the high spatial resolution of MRI, enhancement of MRI-based temporal resolution up to that of EEG or MEG on the order of milliseconds is imperative to advance the understanding of the brain in vivo.

Many attempts have been made to use MRI to directly image neuronal activity (8). Most of them were based on the neuronal current models, where neuronal currents flowing along the axon produce an ultraweak circumferential magnetic field on the order of nanotesla (nT) (9, 10), thereby locally changing the phase and magnitude of magnetic resonance (MR) signals. Phantom studies demonstrated small phase shifts ($<1^\circ$) induced by magnetic field changes ≤ 1 nT when injecting electrical currents through wires in a gel phantom (9, 11–13). In vitro studies using hemoglobin-free biological objects (14–18) also reported changes in the magnitude of MR signals (e.g., 0.01 to 5.5%) induced by the applied stimulus. Some studies have argued that they succeeded in directly detecting human brain activation in vivo (19–24), but these results have not been replicated in later attempts (25–29).

Other attempts have also been made to directly measure neuronal activity using biophysical changes at the cellular level or by using contrast agents. In diffusion fMRI, microstructural changes such as cell swelling, which may cause changes in water diffusion, have been proposed as possible signal sources for directly measuring neuronal activity (30–33). Although initial results were called into question (32), more recent work has shown encouraging evidence that diffusion fMRI provides faster and more-specific detection of neuronal activity than conventional fMRI on the basis of hemodynamic responses (33). Another approach is the development of contrast agents such as manganese that enable in vivo measurements of intracellular calcium in rodents (34) but are limited by toxicity and induced physiological effects, particularly in human studies.

We propose a method to enable direct imaging of neuronal activity (hereafter referred to as DIANA) for functional MRI. With DIANA, the temporal resolution is increased up to

the temporal precision of neuronal activity in milliseconds while retaining the original benefit of the high spatial resolution of MRI.

Results

MRI of neuronal activity at millisecond temporal resolution

To implement high temporal resolution at the millisecond scale, we used a conventional two-dimensional (2D) gradient-echo imaging sequence with a short echo time (TE) and short repetition time (TR) of a few milliseconds by combining a line-scan acquisition strategy (35–37), which will be referred to as 2D fast line-scan, where a single line of k -space was repeatedly acquired during each interstimulus interval and different k -space lines were acquired in different periods. Each stimulation period adds one line of the k -space to all the time-series images within the period (Fig. 1A), and the TR exactly determines the temporal resolution of the dynamic imaging. This can be implemented simply by swapping the order of repetition and phase-encoding loops in a 2D gradient-echo imaging sequence (35, 36). Electrical stimulation was repeatedly applied at 200-ms interstimulus intervals, determined by 5-ms TR multiplied by 40 frames in the time series. The TE for each line scan was set as short as 2 ms. We delivered electrical stimulation to the left whisker pad (strength, 0.5 mA; duration, 0.5 ms; frequency, 5 Hz) of anesthetized mice placed inside the 9.4-T scanner and imaged a single 1-mm coronal brain slice containing the right barrel field of the primary somatosensory cortex (S1BF) (Fig. 1B). In response to the electrical whisker-pad stimulation, a statistically significant increase in the DIANA signal was observed in the contralateral S1BF compared with the prestimulus signal ($0.169 \pm 0.011\%$, $p < 0.001$, five mice) (Fig. 1, C to E, and fig. S1), whereas there were no significant changes in unstimulated control mice or postmortem mice (Fig. 1, C to E, and fig. S1) or in sham experiments performed using an agar phantom (fig. S2). The peak DIANA signal occurred with a latency of 25.00 ± 1.58 ms after the electrical whisker-pad stimulation onset (Fig. 1, C, D, and F), indicating that 2D fast line-scan can detect whisker-pad stimulation-evoked responses by achieving high temporal resolution in the millisecond range. To find the neural correlates of the DIANA response in vivo, the same electrical whisker-pad stimulation paradigm as in Fig. 1B was repeated but now in mice implanted with a 32-channel silicon probe in the S1BF (Fig. 1G) to record the local field potential (LFP) and single-unit spike activities (Fig. 1H), from which their latencies were analyzed (Fig. 1, I to K). The peak of whisker-pad stimulation-evoked LFP had a latency of 39.48 ± 1.84 ms (12 mice), which was significantly slower than the latency of the DIANA response ($p < 0.001$; Fig. 1, I and K). However,

¹Department of Biomedical Engineering, Sungkyunkwan University, Suwon 16419, Republic of Korea. ²Department of Intelligent Precision Healthcare Convergence, Sungkyunkwan University, Suwon 16419, Republic of Korea. ³Department of Brain and Cognitive Engineering, Korea University, Seoul 02841, Republic of Korea. ⁴Division of Computer Engineering, Baekseok University, Cheonan 31065, Republic of Korea. ⁵Department of Electrical and Computer Engineering, Seoul National University, Seoul 08826, Republic of Korea.

⁶Department of Biomedical Engineering, Ulsan National Institute of Science and Technology, Ulsan 44919, Republic of Korea. ⁷Department of Brain and Cognitive Sciences, Seoul National University, Seoul 08826, Republic of Korea.

*Corresponding author. Email: jyparu@skku.edu (J.-Y.P.); jkwag@snu.ac.kr (J.K.).
†These authors contributed equally to this work.

‡Present address: GE Global Research, Niskayuna, NY 12309, USA.

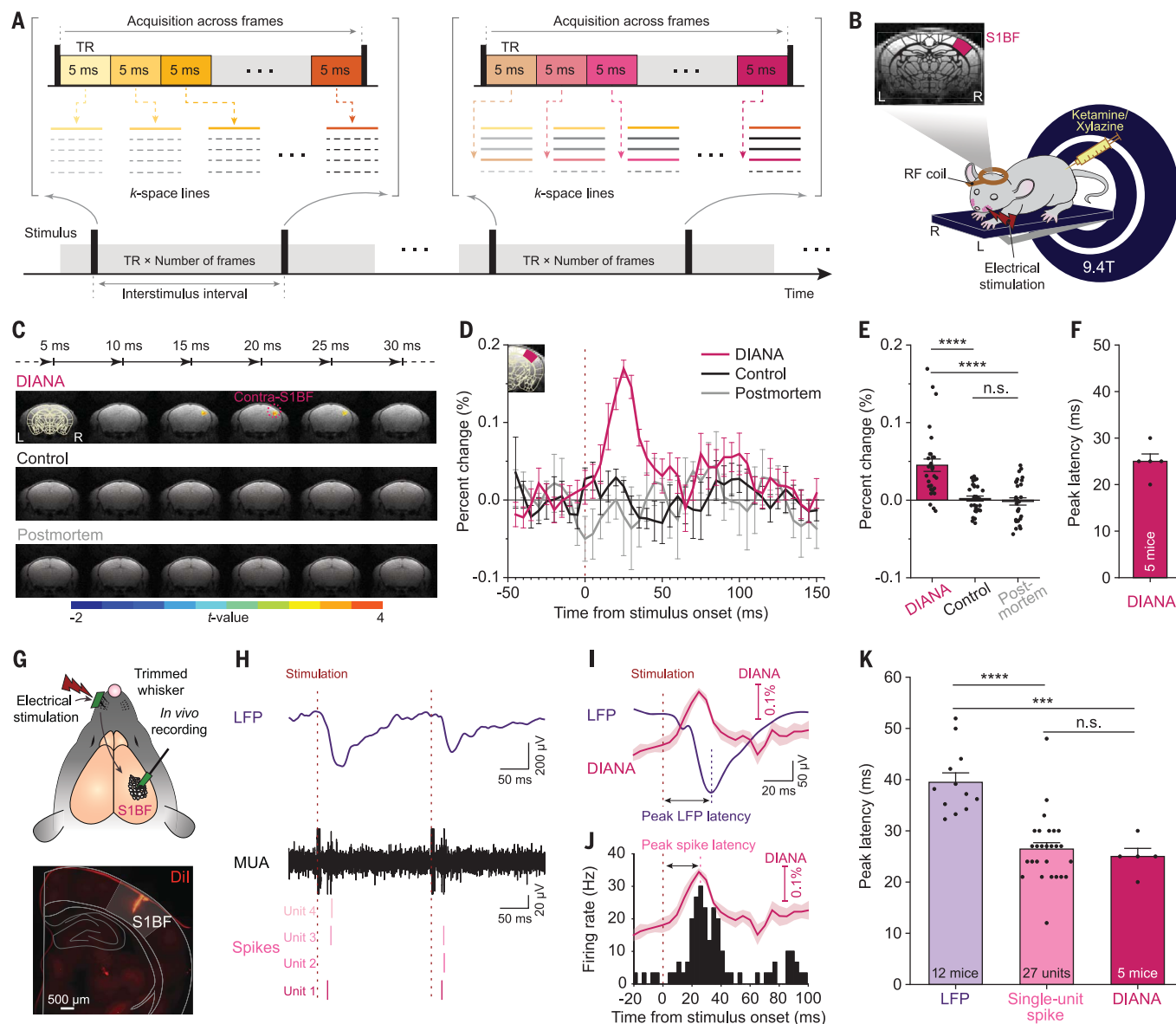


Fig. 1. Direct imaging of neuronal activity with high spatiotemporal resolution. (A) 2D fast line-scan DIANA (direct imaging of neuronal activity) acquisition scheme. (B) Illustration of the DIANA experiment used to image the S1BF by applying electrical stimulation to the left whisker pad in an anesthetized mouse on a 9.4-T scanner. L, left; R, right; RF, radiofrequency. (C to E) Time series of *t*-value maps at 5-ms temporal resolution (C), percent changes in DIANA signals (D), and mean signal changes during poststimulation (E) with electrical whisker-pad stimulation (magenta, $n = 5$ mice) and without stimulation (control, black, $n = 5$ mice) and in the postmortem condition (gray, $n = 4$ mice). In (D), the inset shows the contralateral S1BF. (F) Latency of the peak DIANA response. (G) Electrophysiological recording in mice in vivo with a 32-channel silicon probe implanted in the contralateral S1BF applying electrical whisker-pad stimulation (top) and electrode track marking using a fluorescent lipophilic

dye (Dil) (bottom). (H) LFP signal (purple trace, top) and MUA (black trace, middle) from which single-unit spikes (bottom) were analyzed. Spikes of each single unit are displayed in different shades of magenta. (I and J) LFP (I) and PSTH of the whisker-pad stimulation-responsive single units over time in the contralateral S1BF (J) with DIANA signals superimposed (magenta trace) for comparison. (K) Bar graph showing the latencies of LFP (purple, $n = 12$ mice), the peak spike firing rate of whisker-pad stimulation-responsive single units (light magenta, $n = 27$ units from 10 mice), and the DIANA response (magenta, $n = 5$ mice). Vertical dashed lines indicate the electrical whisker-pad stimulation onset time [(D) and (H) to (J)] and latency of either peak LFP (I) or peak spike firing rate (J). All data are means \pm SEM. *** $p < 0.001$, **** $p < 0.0001$, and n.s. is $p > 0.05$ for Kruskal-Wallis analysis of variance (ANOVA) with Dunn post hoc test (E) and one-way ANOVA with Bonferroni post hoc test (K).

the peak spike firing rates of whisker-pad stimulation-responsive single units had a latency of 26.44 ± 1.24 ms (27 units from 10 mice) in the poststimulus time histogram (PSTH) (Fig. 1J), which was similar to the DIANA re-

sponse latency (Fig. 1K). Other temporal spike characteristics such as time-to-first spike latency as well as median and mode of whisker-pad stimulation-responsive spike timings were also similar to the DIANA response

latency (fig. S3). Both DIANA response amplitudes and spike firing rates increased with increasing strength of electrical whisker-pad stimulation, with little change in the latencies of their peaks (fig. S4).

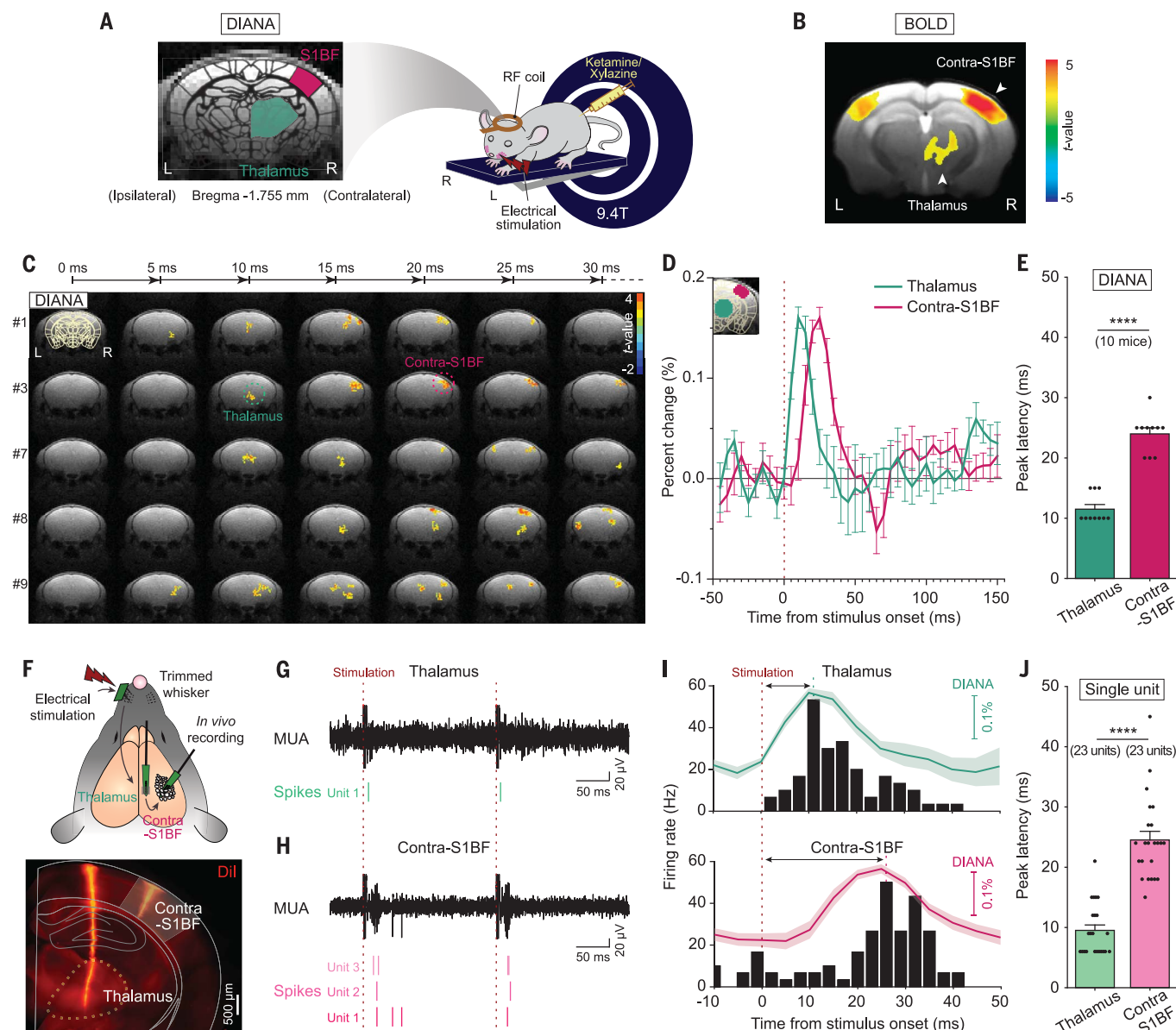


Fig. 2. High temporospatial resolution DIANA captures thalamocortical spike propagation. (A) Illustration of the DIANA experiment to image the contralateral S1BF and thalamus by applying electrical stimulation to the left whisker pad in an anesthetized mouse on a 9.4-T scanner (right) and brain imaging of a coronal slice containing both thalamus and S1BF regions (left). (B) BOLD activation map obtained as a reference ($n = 10$ mice). (C to E) Time series of t -value maps of DIANA for 30 ms after electrical whisker-pad stimulation in 5-ms temporal resolution from five mice (C), percent changes in DIANA signals (D), and a bar graph showing the mean latencies of peak DIANA responses from the thalamus (green) and contralateral S1BF (magenta) (E) ($n = 10$ mice, **** $p < 0.0001$ for paired Student's t test). (F) Illustration of electrophysiological recording in mice in vivo with silicon probes implanted in the thalamus and contralateral S1BF applying electrical whisker-pad

stimulation (top) and electrode track marking using a fluorescent lipophilic dye (Dil) (bottom). (G and H) MUA (black trace, top) from which single-unit spikes (bottom) were analyzed in the thalamus (green) (G) and the contralateral S1BF (magenta) (H). (I) PSTH of the whisker-pad stimulation-responsive single units over time in the thalamus (top) and contralateral S1BF (bottom) with DIANA signals superimposed for comparison. (J) Bar graph showing the latencies of peak spike firing rates of whisker-pad stimulation-responsive single units recorded from the thalamus (light green, $n = 23$ units from 10 mice) and contralateral S1BF (light magenta, $n = 23$ units from five mice) (**** $p < 0.0001$ for unpaired Student's t test). Vertical dashed lines indicate the electrical whisker-pad stimulation onset time (red) [(D) and (G) to (I)] and latency of peak spike firing rate (thalamus, green; contralateral S1BF, magenta) (I). All data are means \pm SEM.

Temporospatial imaging of neuronal activity propagation

Because somatosensory stimulus-evoked spikes propagate to the S1BF via the thalamus (38), we next explored whether the high temporospatial resolution (5 ms, 0.22 mm) of the 2D fast line-scan could also capture the propagation of spikes.

When a 1-mm coronal brain slice containing both the thalamus and S1BF was imaged by applying electrical whisker-pad stimulation (Fig. 2A), conventional BOLD-fMRI showed concomitant activation of the thalamus and contra- and ipsilateral S1BF (Fig. 2B and fig. S5). However, DIANA showed statistically significant responses

that were sequentially activated in the order of the thalamus, contralateral S1BF, and ipsilateral S1BF (Fig. 2, C and D, and fig. S6, A and B) with latencies of 11.50 ± 0.76 , 24.00 ± 1.00 , and 28.50 ± 3.08 ms, respectively (Fig. 2E and fig. S6C; 10 mice). Further cross-correlation analysis of the time series confirmed that

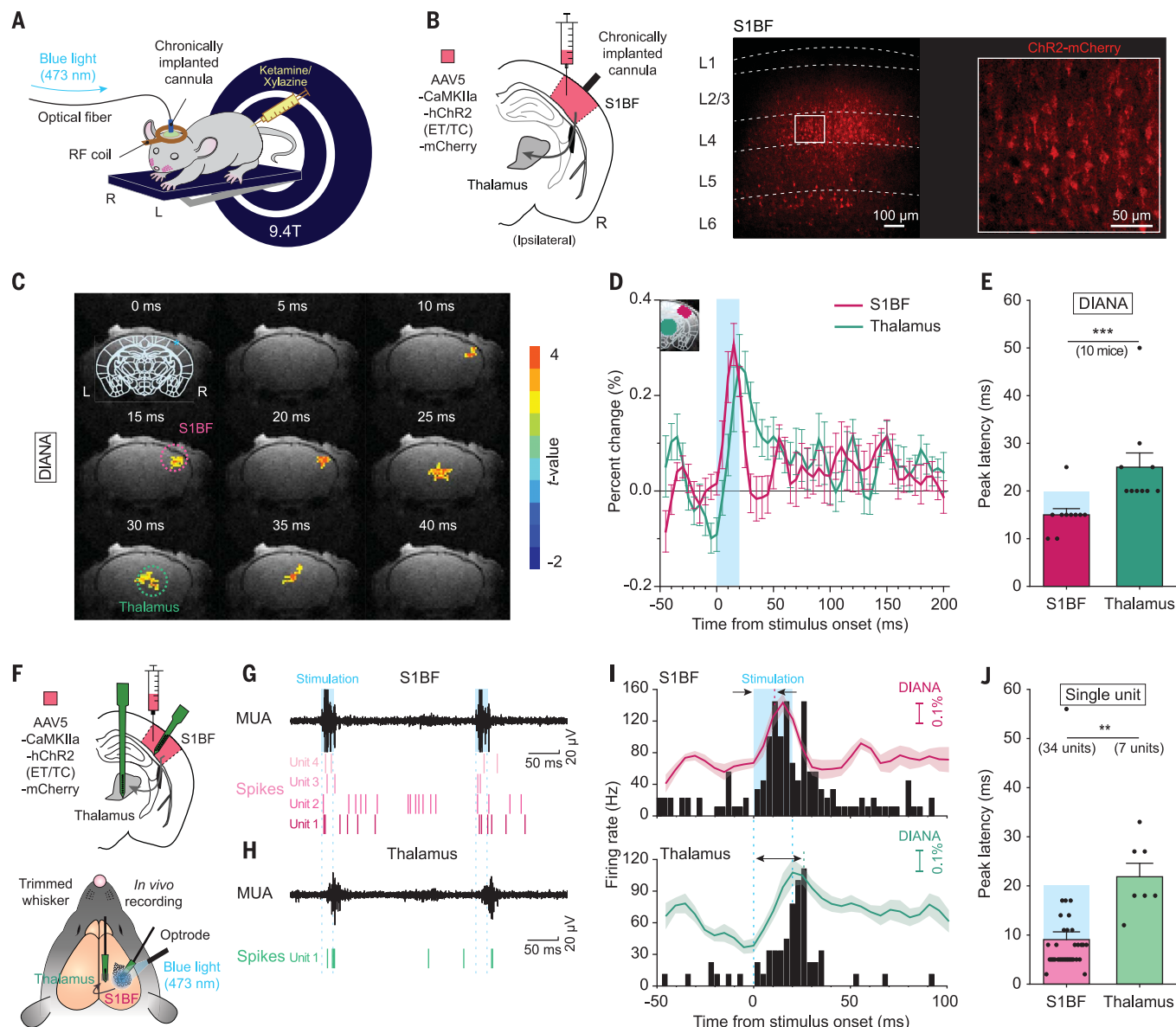


Fig. 3. Optogenetic DIANA experiment: DIANA responses directly detect optogenetic stimulation-evoked spikes. (A) Illustration of the optogenetic DIANA experiment where a fiberoptic cannula is implanted in the mouse S1BF for blue-light (473 nm) stimulation. (B) Illustration of injection of AAV5-CaMKIIa-hChR2 (ET/TC)-mCherry in S1BF (left), which expressed ChR2 to excitatory neurons across all layers of the S1BF. Confocal imaging of mCherry-expressing excitatory neurons (right). (C) Time series of *t*-value maps of DIANA from the S1BF and thalamus of a mouse (cluster size >5 voxels) imaged for 40 ms after blue-light stimulation onset (intensity, 50 mW/mm²; duration, 20 ms). (D and E) Percent changes in DIANA signals (D) and bar graph showing the mean latencies of peak DIANA responses in the contralateral S1BF (magenta) and thalamus (green) (E) (*n* = 10 mice, ****p* < 0.001 for paired Student's *t* test). Blue shading indicates the period of blue-light

stimulation. (F) Illustration of simultaneous electrophysiological recordings in vivo in the thalamus and S1BF in mice injected with AAV5-CaMKIIa-hChR2(ET/TC)-mCherry in the S1BF, using the same blue-light stimulation as in the optogenetic DIANA experiment. (G and H) MUA (black trace, top) from which single-unit spikes (bottom) were analyzed in the contralateral S1BF (G) and the thalamus (H). (I) PSTH of the blue-light stimulation-responsive single units over time in the S1BF (top) and thalamus (bottom) with DIANA signals superimposed for comparison. (J) Bar graph showing the latencies of peak spike firing rates after the blue-light stimulation in the S1BF (*n* = 34 units from eight mice) and thalamus (*n* = 7 units from four mice) (***p* < 0.01 for unpaired Student's *t* test). Blue shading and vertical dashed lines indicate the period of optogenetic stimulation in the S1BF [(D), (E), and (G) to (J)]. All data are means ± SEM.

thalamic responses precede contra- and ipsilateral S1BF responses by 10 to 15 ms (fig. S7). To determine whether the temporospatial propagation of the DIANA response matches that of spikes in the thalamocortical pathway, we performed simultaneous single-unit recordings in the thalamus and S1BF using two silicon probes

(Fig. 2, F to I). Latencies of peak spike firing rates of the whisker-pad stimulation-responsive single units occurred in the order of the thalamus (9.52 ± 0.90 ms, 23 units from 10 mice), contralateral S1BF (24.52 ± 1.43 ms, 23 units from five mice) (Fig. 2, I and J), and ipsilateral S1BF (30.00 ± 1.73 ms, three units from one mouse)

(fig. S8). Such sequential propagation of spikes in the thalamus and S1BF was statistically similar to that observed from the DIANA response (Fig. 2E and fig. S9). LFPs also showed sequential propagation in the thalamus (31.78 ± 3.67 ms), contralateral S1BF (42.69 ± 3.04 ms), and ipsilateral S1BF (57.67 ± 5.33 ms), but they

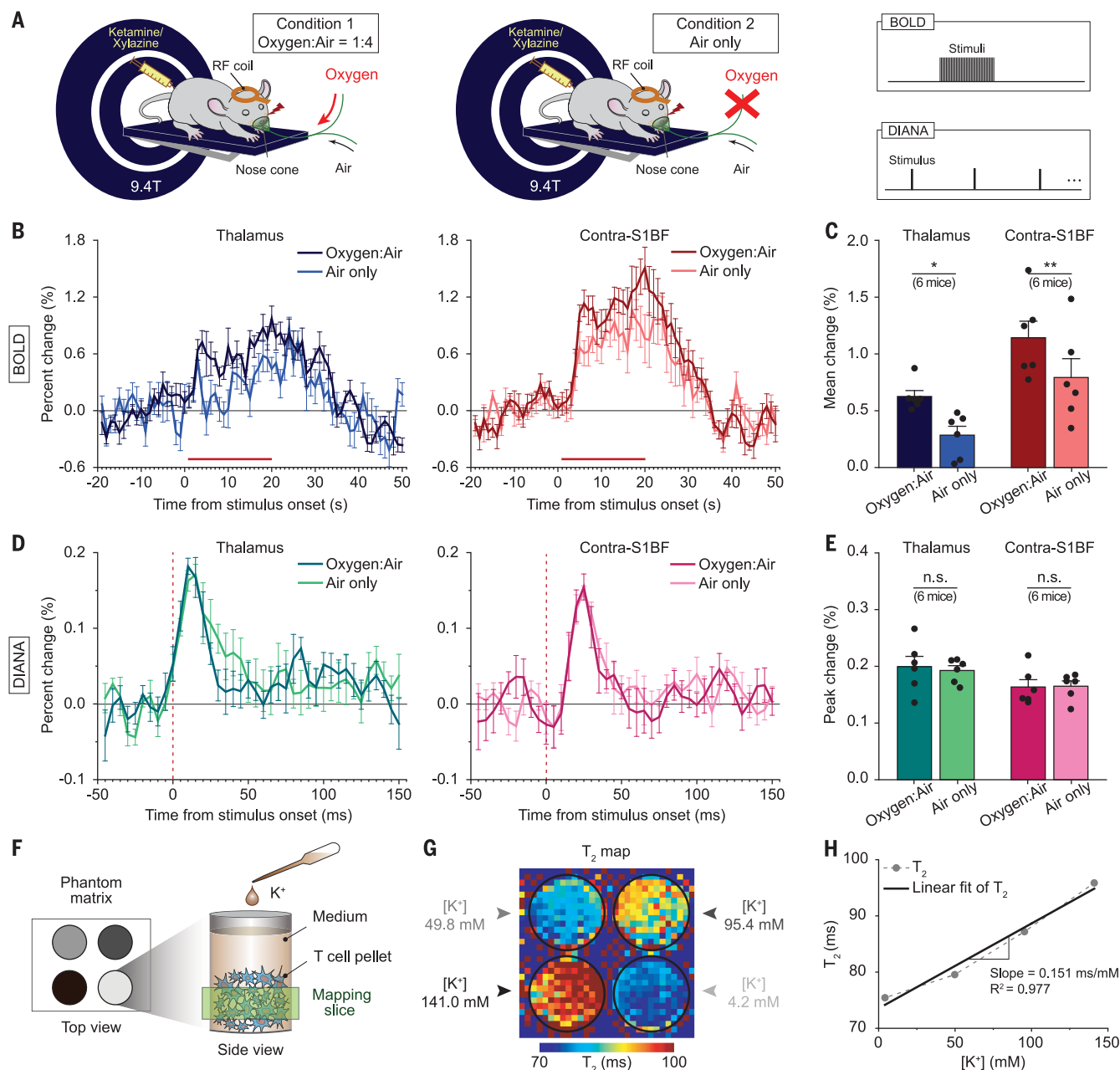


Fig. 4. BOLD-suppressed DIANA using 2D fast line-scan and its hypothesized contrast mechanism. (A) Illustration of oxygen challenge BOLD-fMRI and DIANA experiments to image contralateral S1BF and thalamus by applying electrical stimulation to the left whisker pad in an anesthetized mouse on a 9.4-T scanner under two conditions: one condition as a default with a mixture of extra oxygen and air (1:4) (left) and the other condition with air only (middle) at the same flow rate. The same whisker-pad electrical stimulus (strength, 0.5 mA; pulse duration, 0.5 ms) was used for both BOLD and DIANA stimulation paradigms (right). (B and C) Percent signal changes of BOLD responses obtained from the thalamus [(B), left] and contralateral S1BF [(B), right] under two conditions and the

corresponding bar graph showing the mean signal changes of BOLD responses in the thalamus and contralateral S1BF [(C); $n = 6$ mice]. The horizontal red bar indicates the period of electrical stimulation in BOLD-fMRI. (D and E) Same as (B) and (C) but with responses acquired using DIANA ($n = 6$ mice). Vertical dashed lines indicate the stimulation onset time. (F) Illustration of a phantom experiment using T cells. (G) T_2 relaxation time maps acquired at different extracellular $[K^+]$ from normal to depolarized states ranging from 4.2 to 141.0 mM. (H) Plot of T_2 (dashed line) changes with respect to $[K^+]$. The solid line is a linear fit to the T_2 values to calculate the correlation coefficient with respect to $[K^+]$. All data are means \pm SEM. $*p < 0.05$, $**p < 0.01$, and n.s. is $p > 0.05$ for paired Student's t test.

were significantly slower than the DIANA response (fig. S9).

Optogenetic DIANA experiment

Although the temporal characteristics of DIANA responses and electrophysiologically recorded

spikes in vivo are statistically similar, these measurements are somewhat limited because they were not measured simultaneously. To more directly verify that DIANA using 2D fast line-scan is capable of imaging spike activity in vivo, we used an optogenetic fMRI scheme. DIANA

responses were measured during optogenetic activation of channelrhodopsin2 (ChR2)-expressing excitatory neurons in the S1BF with 473-nm blue light delivered through a chronically implanted fiberoptic cannula (Fig. 3A). Immunostaining showed ChR2-mCherry expression

in excitatory neurons across all cortical layers of the SIBF (Fig. 3B). During blue-light stimulation (intensity, 50 mW/mm²; duration, 20 ms), DIANA responses were acquired as a time series of 50 images every 5 ms from a 1-mm coronal brain slice containing both the thalamus and SIBF (Fig. 3C). We found statistically significant DIANA signal changes in the SIBF with peak response latencies of 15.00 ± 1.29 ms, which were followed by significant DIANA signal changes in the thalamus with peak response latencies of 25.00 ± 2.98 ms after light stimulation onset (Fig. 3, D and E; 10 mice). Blue-light stimulation alone in control mice or Chr2 expression alone without blue-light stimulation did not change DIANA signals (fig. S10). When we recorded blue-light stimulation-evoked single-unit activities in the SIBF and thalamus of the same mice used for the optogenetic DIANA experiment (Fig. 3F), the peak spike firing rate of neurons in the SIBF occurred at 9.06 ± 1.59 ms after light stimulation onset (34 units from eight mice), followed by the thalamic peak spike firing rate occurring at 21.86 ± 2.76 ms (seven units from four mice) (Fig. 3, G to I), showing feedback spike propagation in the corticothalamic pathway. Both the DIANA response and the peak spike firing rate increased with increasing blue-light stimulation duration (fig. S11), indicating a similarity between the DIANA responses and single-unit activity. LFP also captured the blue-light stimulation-induced feedback activation in the corticothalamic pathway (fig. S12), with peak LFP latencies observed at 22.34 ± 0.87 ms in the SIBF and 77.47 ± 4.60 ms in the thalamus, respectively, after blue-light stimulation onset (fig. S12B). However, the peak LFP latencies were significantly slower than those in response to optogenetic DIANA (fig. S12B).

DIANA response as a non-BOLD effect

It could be possible that DIANA responses obtained from 2D fast line-scan involve hemodynamic responses such as the BOLD effect. To dissociate the BOLD effect from the DIANA response, BOLD-fMRI experiments were performed under two conditions: a default condition with an extra oxygen-to-air ratio of 1:4 (oxygen:air condition) and the other with air only (Fig. 4A). BOLD responses in the thalamus and SIBF after electrical whisker-pad stimulation in the air-only condition were significantly reduced compared with those in the oxygen:air condition (thalamus: $0.626 \pm 0.052\%$ to $0.284 \pm 0.079\%$; contralateral SIBF: $1.142 \pm 0.147\%$ to $0.792 \pm 0.166\%$; Fig. 4, B and C), consistent with the dependence of BOLD activation on oxygen supply (39, 40). By contrast, there was little change in the DIANA response between the oxygen:air and air-only conditions (thalamus: 0.199 ± 0.018 to $0.193 \pm 0.008\%$; contralateral SIBF: $0.164 \pm 0.013\%$ to $0.165 \pm 0.009\%$; Fig. 4, D and E).

With respect to the data acquisition scheme, theoretical analysis revealed that the BOLD effect is suppressed by the TE/T_2^* ratio because of the short TE compared with that of conventional BOLD-fMRI, where $TE \approx T_2^*$ (T_2^* , effective spin-spin relaxation time; see methods for details). For example, assuming that $T_2^* = 20$ ms in the mouse brain and TE is set to 2 ms, the BOLD effect of the 2D fast line-scan experiment is reduced to 1/10 compared with that of BOLD-fMRI (fig. S13). The BOLD effect is further suppressed because of the fast, event-synchronized line-scan acquisition with a relatively short interstimulus interval compared with slow-varying hemodynamic responses of several seconds. In this case, the BOLD signal is suppressed by a factor of $(N - 1)/MN \approx 1/M$ (N , number of frames in interstimulus interval; M , number of phase-encoding steps) across all frames (see methods for details). For example, for $N = 40$ and $M = 54$, as in our DIANA experiment, the BOLD effect is further reduced by a factor of 0.018 (fig. S13). These theoretical analysis results were confirmed through numerical simulations (fig. S14). Furthermore, in terms of signal source, the BOLD signal is reported to be as small as $\sim 0.021\%$ during high-frequency stimulation that oscillates at 0.75 Hz at 7 T (2), which predicts that it might be much smaller and negligible for 5-Hz stimulation, as in this study.

What could be the possible signal source of the DIANA response? Electromagnetic effects based on popular neuronal current models cannot be a candidate because signal loss caused by the phase cancellation of proton spins under the neuronal current-induced magnetic field change has a negative value (8, 9, 14, 20), whereas the DIANA response has a positive signal change in the main lobe.

Instead, because changes in neuronal membrane potential can induce reorientation of the membrane interfacial water (41), the DIANA response may arise from changes in MR relaxation times such as T_2 relaxation time during neuronal activity, which is closely related to the amount of water molecules in the hydration layer on the membrane surface (42–45) (see supplementary text 1 for details). Changes in T_2 relaxation time may also be attributed to rapid microstructural changes at the cellular level coupled with neural activity such as cell swelling (46), which has been postulated as one of the main signal sources for diffusion MRI (47–50). We performed phantom experiments using T cells to measure T_2 relaxation times while T cell membrane potentials were manipulated by different extracellular K^+ concentrations ($[K^+]$) (51) (4.2 to 141.0 mM in Fig. 4F and 1.0 to 4.2 mM in fig. S15A). We used T cells as the phantom because, unlike neurons, T cells are homogeneous and can survive without an oxygen supply in vitro in the scanner. The T_2 relaxation time map (Fig. 4G) and

values showed a strong positive correlation with $[K^+]$ (T_2 slope of 0.151 ms/mM, coefficient of determination (R^2) = 0.977; Fig. 4H). Thus, it is possible that changes in membrane potential during neuronal activity may account for changes in T_2 .

Based on these measurements of T_2 changes, Bloch simulation was performed to estimate DIANA signal changes and showed a positive signal change of 0.139% in the main lobe (fig. S15, B and C), which is in good agreement with the experimental results (Figs. 1 to 3). The T_2 dependence of the DIANA response was further confirmed by modulating the T_2 weighting with different TEs in the DIANA experiment with the same electrical whisker-pad stimulation (fig. S16, A and B). By contrast, T_1 -dependent changes in the DIANA signal were not observed in experiments where T_1 weighting was modulated with different flip angles (fig. S16, C and D). This is expected because it takes hundreds of milliseconds to several seconds for the T_1 change to manifest itself.

High temporospatial DIANA of neuronal activity propagation in thalamocortical microcircuits

Elucidating how sensory-evoked neural activities propagate across the microcircuits of multiple brain regions for sensory perception is one of the long-standing conundrums in sensory neuroscience. Because our 2D fast line-scan approach can directly image neural activities with not only high temporal resolution (5 ms) but also fine spatial resolution (0.22 mm) that can capture microstructures of the cortex and thalamus, we were able to address this question. We selected regions of interest (ROIs) from the thalamus, SIBF, and secondary somatosensory cortex (S2) (Fig. 5A). Within the ROIs, the thalamus was subdivided into the posterior medial (POm) group, the ventral part of the ventral posteromedial nucleus (VPMv), and the dorsal part of the VPM (VPMd), whereas the SIBF and S2 were anatomically divided into cortical layers L2/3, L4, L5, and L6 (Fig. 5A). From these 11 ROIs, the DIANA data acquired during electrical whisker-pad stimulation were reanalyzed. For comparison, we also performed in vivo single-unit spike recordings in the corresponding thalamocortical microcircuits (Fig. 5B and fig. S17).

Heatmaps and percent changes of DIANA signals in response to electrical whisker-pad stimulation revealed distinct temporospatial neural activity propagation characteristics across the subdivisions of the thalamus and the cortical layers of the SIBF and S2 that were similar to those observed with single-unit spikes recorded in vivo (Fig. 5, C to H, and fig. S18). In the thalamus, both peak DIANA signals and peak spike firing rates were initiated from the VPMv, followed by the POm and VPMd (Fig. 5, C and D). In the SIBF, both

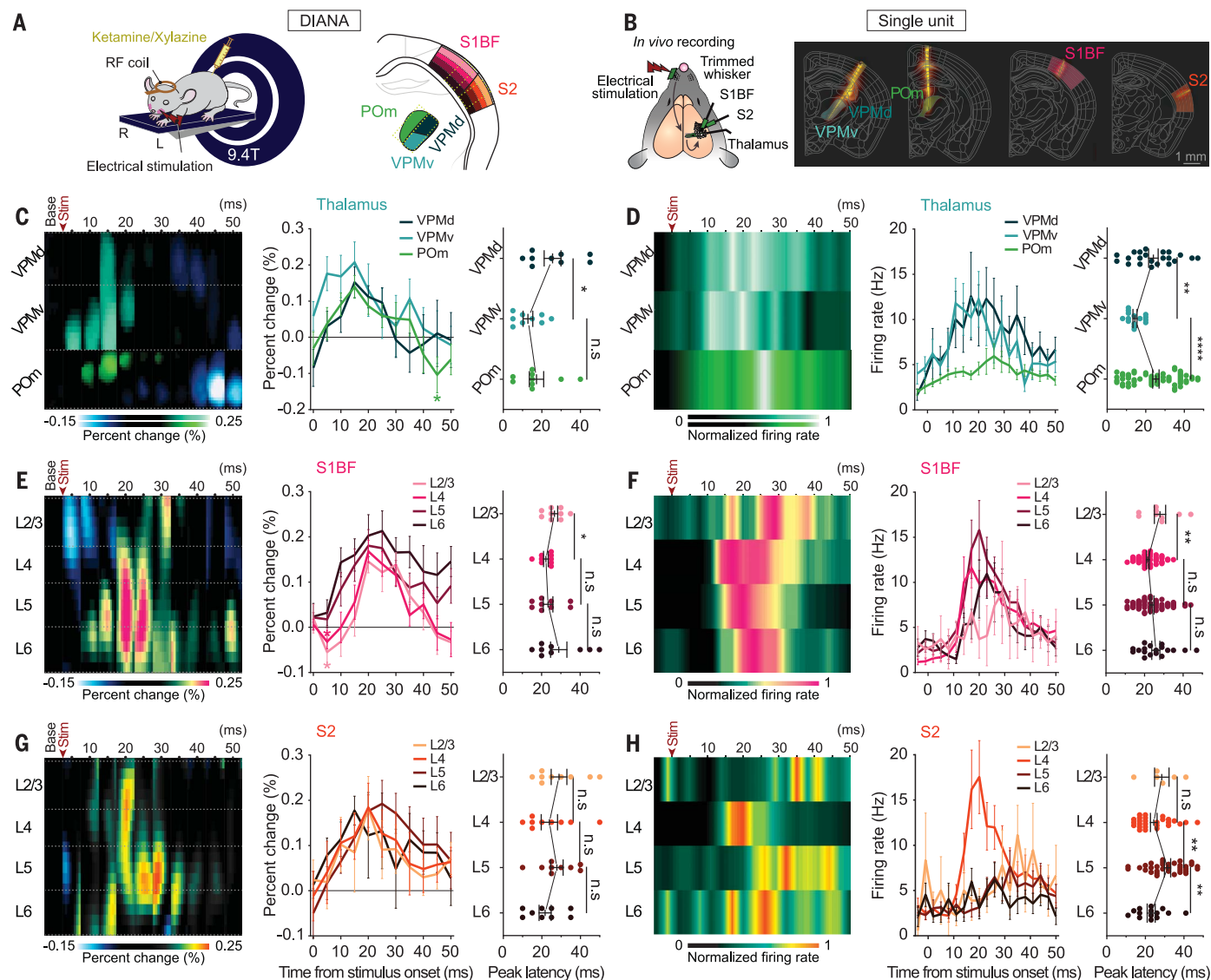


Fig. 5. Sublayer-specific DIANA responses reveal functionally distinct sublayer-specific microcircuits. (A and B) Illustration of the DIANA experiment (A) and in vivo spike recording (B) in the VPMd, VPMv, POM, S1BF, and S2 in response to electrical whisker-pad stimulation. Yellow dotted boxes in [(A), right] indicate extraction areas of DIANA heatmaps. (C) Heatmap (left) and temporal profile (middle) for the percent change in the DIANA signal, displayed with the mean latency of peak DIANA response from the VPMd (dark green), VPMv (green), and POM (light green) (right) ($n = 9$ mice). (D) Heatmap of in vivo-recorded single-unit spike firing rate normalized to the peak spike firing rate (left) and temporal profile of spike firing rate (middle), displayed with the mean latency of peak spike firing rate in the VPMd (dark green, $n = 22$ units from 16 mice), VPMv (green, $n = 15$ units from 16 mice), and POM (light green,

$n = 59$ units from 14 mice) (right). (E and F) Same as (C) and (D) but for DIANA experiments ($n = 9$ mice) and spikes recorded from S1BF in L2/3 (light pink, $n = 9$ units from 28 mice), L4 (pink, $n = 51$ units from 28 mice), L5 (magenta, $n = 60$ units from 28 mice), and L6 (dark magenta, $n = 18$ units from 28 mice). (G and H) Same as (C) and (D) but for DIANA experiments ($n = 9$ mice) and spikes recorded from S2 in L2/3 (light orange, $n = 6$ units from 20 mice), L4 (orange, $n = 27$ units from 20 mice), L5 (brown, $n = 35$ units from 20 mice), and L6 (dark brown, $n = 14$ units from 20 mice). The base in DIANA heatmaps indicates the average of prestimulation frames. The asterisk in the middle panels of (C) and (E) indicates the statistically significant negative signal. All data are means \pm SEM. * $p < 0.05$, ** $p < 0.01$, **** $p < 0.0001$, and n.s. is $p > 0.05$ for paired Student's t test, unpaired Student's t test, and Welch's t test.

peak DIANA signals and peak spike firing rates were initiated in L4 and L5, after which they propagated to L6 and L2/3 (Fig. 5, E and F), which is consistent with in vivo observations (52, 53). In S2, for both peak DIANA signals and peak spike firing rates, L4 and L6 were the first layers to be activated, after which L5 and L2/3 were activated (Fig. 5, G and H), showing that neural activity propa-

gation profiles are distinctively different between the S2 and S1BF.

To further investigate the correlation between the temporal dynamics of the DIANA response with neural activity, we analyzed the time point at which 30% of the peak DIANA response and peak spike firing rate occurred (fig. S19), but there were no significant differences (fig. S19). Also, the latencies of peak spike

firing rates of multiunit activities (MUA) were similar to those of DIANA responses (fig. S20).

Although DIANA responses had high temporal correlations with spikes and MUA in all ROIs (Fig. 5 and fig. S20), they may not be detecting spikes per se but instead be detecting depolarizing membrane potential changes, as suggested by the T cell experiments in Fig. 4. Simultaneous intracellular recording of neurons

during DIANA is technically difficult. However, current-source density (CSD) analysis allows the estimation of transmembrane current influx to neurons (current sink) in a layer-specific manner in the cortex (54). Indeed, CSD analysis from our data revealed that the latencies of the first current sink were similar to the latencies of the DIANA response in each layer of the S1BF and S2 (fig. S21), indicating that membrane depolarization caused by the influx of positive ions into neurons in each layer may have been manifested in positive DIANA responses.

The DIANA heatmap also showed two statistically significant negative DIANA percent signal changes that occurred before the peak positive DIANA responses in selected layers of the S1BF and S2 (Fig. 5, C to H, and fig. S22) and after the peak positive DIANA responses in the thalamus, S1BF, and S2 (fig. S22). Because DIANA using 2D fast line-scan can potentially image hyperpolarization of the neural network (fig. S15A), it is possible that γ -aminobutyric acid-containing (GABAergic) inhibitory interneuron-mediated hyperpolarization in excitatory neurons could have been manifested in DIANA responses. Based on the DIANA signals, the sensory input sequentially propagates through the VPMv, POM, and VPMd, after which they are inhibited to ensure that the initial epoch of sensory input can reliably propagate within cortical layers of the S1BF and S2 without being interrupted by other thalamic inputs (Fig. 5, C, E, and G). Also, thalamic input first inhibits L2/3 and L4 of the S1BF, whereas in the S2, L5 is inhibited first, which may contribute to the distinct laminar-specific signal propagation profiles observed in the S1BF and S2 (Fig. 5, C, E, and G). Thus, the DIANA signals observed here may provide the first experimental clues as to how spatiotemporally dynamic excitation and inhibition of neural circuits can route the flow of sensory-evoked signals.

Discussion

Together, our results demonstrate that a 2D fast line-scan approach enables direct mapping of spike activity in vivo with high temporal (5 ms) and spatial (0.22 mm) resolution, as confirmed through in vivo electrophysiology combined with optogenetics. Such high temporal resolution of the 2D fast line-scan DIANA allowed the detection of sequential propagation of neuronal activity through functionally defined neural networks in the thalamocortical and corticothalamic pathways. The 2D fast line-scan DIANA was also able to reveal the temporal neural network dynamics of multiple functionally connected brain regions—such as the thalamus, S1BF, and S2—at the subthalamic nucleus and cortical layer level.

In 2D fast line-scan DIANA, millisecond temporal resolution is a pivotal factor in direct measurement of neuronal activity because it

helps to effectively capture the transient effects of neuronal activity in milliseconds. The DIANA response decreases with decreasing temporal resolution (fig. S23). This explains why the DIANA response has not been seen in previous fMRI studies with high temporal resolution, including line scan-based fMRI studies with the highest temporal resolution of 40 to 50 ms (fig. S24) (35, 55). No DIANA response is shown even in single-shot single-slice echo planar imaging with the shortest achievable acquisition time of 20 to 30 ms (fig. S25). Another important feature of 2D fast line-scan DIANA is the ability to effectively suppress the BOLD effect (2) with its distinctive data acquisition scheme that uses the fast, event-synchronized line-scan with short TEs of a few milliseconds and a relatively short interstimulus interval (figs. S13 and S14).

The DIANA signal has a higher temporal correlation with the spikes than with the LFP (Figs. 1, I and J, 2I, and 3I), which suggests that DIANA might be detecting signals induced by flows of currents that evoke spikes rather than LFP. Typically, the LFP voltage is generated by the sum of influx and efflux currents across multiple neurons in the extracellular space, so the voltage is in the μ V range (54). By contrast, the changes in membrane potential of individual neurons and their spikes are in the mV range, which is 10^3 times greater than that of the LFP. The DIANA signal could capture changes in membrane voltage on the mV scale, as shown in the T cell experiment in Fig. 4, where an extracellular $[K^+]$ change of 5 to 145 mM corresponds to a change in membrane potential from -40 to 10 mV (51). Moreover, both depolarizing and hyperpolarizing membrane potentiation changes could be detected as positive and negative signal changes in DIANA using 2D fast line-scan (Figs. 4 and 5 and fig. S15). CSD analysis revealed that latencies of the first current sinks had high correlations with latencies of peak positive DIANA responses (fig. S21). It is not possible to relate negative signal changes in DIANA to CSD analysis results (54). However, fast-spiking GABAergic interneurons and somatostatin-positive interneurons that hyperpolarize excitatory neurons have been reported to spike at two distinct time points during somatosensory information processing in the S1BF (56), similar to the two distinct time points observed from negative DIANA responses (fig. S22). The relationship between GABAergic interneuron activity and negative DIANA responses needs further investigation in the future. Nevertheless, these results together support our hypothesis that DIANA signals may be attributed to changes in neuronal membrane potential at the mV scale manifested by changes in transmembrane current flow.

DIANA using 2D fast line-scan has some limitations at this stage. Because 2D fast line-scan DIANA data are only generated in event-related

responses to repetitive stimulation in the line-scan acquisition scheme, it is challenging to investigate brain function in the resting state or with a single stimulus. Moreover, 2D fast line-scan DIANA assumes that event-related responses in the brain are consistent across all responses without trial-by-trial variability, which can somewhat undermine the reliability of DIANA even with a modest change in neural spiking with each stimulation (57). Further investigation is also needed to fully elucidate the mechanism of the DIANA contrast obtained from 2D fast line-scan. In other words, further validation with neurons in vivo is necessary because we hypothesized that the DIANA signal originates from changes in T_2 that are due to changes in membrane potential, which is supported by in vitro T cell experiments and simulations. Two possible mechanisms for these changes in T_2 , that is, changes in hydration water of the plasma membrane and changes in microstructures at the cellular level such as cell swelling, require further investigation to assess their respective contributions.

There are interesting topics that can immediately be explored with DIANA. One is to test its feasibility for human fMRI and to translate DIANA into a clinical human system. Approximate predictions that only take into account neuronal density, magnetic field strength, and typical voxel size in the animal and human systems suggest that DIANA is likely to work in human studies as well (see supplementary text 2). More complicated feedforward and feedback responses are expected to be observed in human brain networks (58), which could make the DIANA response more challenging and even more interesting. However, motion artifacts can be more severe in humans than in anesthetized mice, leading to some inconsistencies in k -space and changes in the steady state of the magnetization.

Another interesting topic to investigate is the rapid dynamics of neural networks other than the somatosensory network presented here, such as the visual or auditory network, in multiple functionally connected distant brain regions (59). Because all experiments in this study were performed with electrical whisker-pad stimulation, which is an experimental paradigm that cannot be applied in human studies, the validation of DIANA experiments using standard visual or auditory stimulation is important to provide a realistic picture of how DIANA can contribute to human studies. A preliminary DIANA experiment with a flashing-light stimulus demonstrates the feasibility of visual stimuli DIANA experiments (fig. S26), exhibiting sequential propagation DIANA responses in the mouse cortex in the order of the superior colliculus (SC), primary visual cortex (V1), and lateral part of the secondary visual cortex (V2L). Although we presented the DIANA data that detect only

fast-phasic neuronal activity here, by adjusting the interstimulus interval long enough to measure the neuronal activity of interest, DIANA could also be used to measure diverse temporal patterns of neuronal activity on various time scales such as sustained tonic neuronal activity over a longer period of time.

Overall, we expect high-resolution DIANA to open up new avenues in neuroimaging for a more accurate and deeper understanding of the brain's functional organization. In particular, the convergence of high temporal and spatial resolution realized through DIANA could help elucidate the causal relationship between temporal and spatial dynamics of neural networks and their functions.

REFERENCES AND NOTES

1. S. Ogawa, T. M. Lee, A. R. Kay, D. W. Tank, *Proc. Natl. Acad. Sci. U.S.A.* **87**, 9868–9872 (1990).
2. L. D. Lewis, K. Setsompop, B. R. Rosen, J. R. Polimeni, *Proc. Natl. Acad. Sci. U.S.A.* **113**, E6679–E6685 (2016).
3. A. Maier et al., *Nat. Neurosci.* **11**, 1193–1200 (2008).
4. Y. B. Sirotnin, A. Das, *Nature* **457**, 475–479 (2009).
5. P. O'Herron et al., *Nature* **534**, 378–382 (2016).
6. Y. B. Sirotnin, E. M. C. Hillman, C. Bordier, A. Das, *Proc. Natl. Acad. Sci. U.S.A.* **106**, 18390–18395 (2009).
7. D. Cohen, *Science* **161**, 784–786 (1968).
8. P. A. Bandettini, N. Petridou, J. Bodurka, *Appl. Magn. Reson.* **29**, 65–88 (2005).
9. J. Bodurka, P. A. Bandettini, *Magn. Reson. Med.* **47**, 1052–1058 (2002).
10. D. Konn, P. Gowland, R. Bowtell, *Magn. Reson. Med.* **50**, 40–49 (2003).
11. M. Singh, *IEEE Trans. Nucl. Sci.* **41**, 349–351 (1994).
12. J. Bodurka et al., *J. Magn. Reson.* **137**, 265–271 (1999).
13. P. Sundaram et al., *Neuroimage* **132**, 477–490 (2016).
14. N. Petridou et al., *Proc. Natl. Acad. Sci. U.S.A.* **103**, 16015–16020 (2006).
15. C. Park et al., *Neuroreport* **15**, 231–234 (2004).
16. T. S. Park, S. Y. Lee, J.-H. Park, M. H. Cho, S. Y. Lee, *Physiol. Meas.* **27**, 181–190 (2006).
17. Q. Luo et al., *Neuroimage* **47**, 1268–1276 (2009).
18. X. Jiang et al., *Magn. Reson. Med.* **72**, 1311–1319 (2014).
19. M. Joy, G. Scott, M. Henkelman, *Magn. Reson. Imaging* **7**, 89–94 (1989).
20. J. Xiong, P. T. Fox, J.-H. Gao, *Hum. Brain Mapp.* **20**, 41–49 (2003).
21. L. S. Chow, G. G. Cook, E. Whitby, M. N. J. Paley, *Neuroimage* **30**, 835–846 (2006).
22. L. S. Chow, G. G. Cook, E. Whitby, M. N. J. Paley, *Magn. Reson. Imaging* **24**, 681–691 (2006).
23. L. S. Chow, G. G. Cook, E. Whitby, M. N. J. Paley, *J. Magn. Reson. Imaging* **26**, 265–273 (2007).
24. L. S. Chow, A. Dagens, Y. Fu, G. G. Cook, M. N. J. Paley, *Magn. Reson. Med.* **60**, 1147–1154 (2008).
25. R. Chu et al., *Neuroimage* **23**, 1059–1067 (2004).
26. L. M. Parkes, F. P. de Lange, P. Fries, I. Toni, D. G. Norris, *Magn. Reson. Med.* **57**, 411–416 (2007).
27. L. Tang, M. J. Avison, J. C. Gatenby, J. C. Gore, *Magn. Reson. Imaging* **26**, 484–489 (2008).
28. J. Huang, *Magn. Reson. Med.* **71**, 756–762 (2014).
29. J. Huang, D. C. Zhu, *Int. J. Imaging Syst. Technol.* **25**, 172–178 (2015).
30. A. Barquie, J. B. Poline, C. Poupon, H. Saint-Jalmes, D. Le Bihan, *Proc. Natl. Acad. Sci. U.S.A.* **98**, 9391–9395 (2001).
31. D. Le Bihan, S. Urayama, T. Aso, T. Hanakawa, H. Fukuyama, *Proc. Natl. Acad. Sci. U.S.A.* **103**, 8263–8268 (2006).
32. K. L. Miller et al., *Proc. Natl. Acad. Sci. U.S.A.* **104**, 20967–20972 (2007).
33. D. Nunes, R. Gil, N. Shemesh, *Neuroimage* **231**, 117862 (2021).
34. A. Rhandov et al., *Nat. Commun.* **10**, 897 (2019).
35. A. C. Silva, A. P. Koretsky, *Proc. Natl. Acad. Sci. U.S.A.* **99**, 15182–15187 (2002).
36. X. Yu et al., *Nat. Methods* **13**, 337–340 (2016).
37. L. Raimondo et al., *J. Cereb. Blood Flow Metab.* **41**, 2831–2843 (2021).
38. E. Ahissar, R. Sosnik, S. Haidarliu, *Nature* **406**, 302–306 (2000).
39. K. M. Sicard, T. Q. Duong, *Neuroimage* **25**, 850–858 (2005).
40. T. Q. Duong, *Brain Res.* **1135**, 186–194 (2007).
41. M. E. P. Didier, O. B. Tarun, P. Jourdain, P. Magistretti, S. Roke, *Nat. Commun.* **9**, 5287 (2018).
42. J. Monroe et al., *Annu. Rev. Chem. Biomol. Eng.* **11**, 523–557 (2020).
43. O. B. Tarun, C. Hanneschläger, P. Pohl, S. Roke, *Proc. Natl. Acad. Sci. U.S.A.* **115**, 4081–4086 (2018).
44. H. T. Edzes, E. T. Samulski, *J. Magn. Reson.* **31**, 207–229 (1978).
45. J. C. Caron, *Biochim. Biophys. Acta* **144**, 1–9 (1967).
46. J. V. Sehy, J. J. H. Ackerman, J. J. Neil, *Magn. Reson. Med.* **48**, 765–770 (2002).
47. I. Pál, G. Nyitrai, J. Kardos, L. Héja, *PLOS ONE* **8**, e57694 (2013).
48. A. El Hady, B. B. Machta, *Nat. Commun.* **6**, 6697 (2015).
49. Y. Yang et al., *ACS Nano* **12**, 4186–4193 (2018).
50. M. Koike-Tani, T. Tominaga, R. Oldenbourg, T. Tani, *bioRxiv* 523571 [Preprint] (2019); <https://doi.org/10.1101/523571>.
51. F. Mello de Queiroz, C. G. Ponte, A. Bonomo, R. Vianna-Jorge, G. Suarez-Kurtz, *BMC Immunol.* **9**, 63 (2008).
52. H. J. Jang et al., *Sci. Adv.* **6**, eaay5333 (2020).
53. C. M. Constantinople, R. M. Bruno, *Science* **340**, 1591–1594 (2013).
54. G. Buzsáki, C. A. Anastassiou, C. Koch, *Nat. Rev. Neurosci.* **13**, 407–420 (2012).
55. X. Yu, C. Qian, D. Y. Chen, S. J. Dodd, A. P. Koretsky, *Nat. Methods* **11**, 55–58 (2014).
56. J. Yu, H. Hu, A. Agmon, K. Svoboda, *Neuron* **104**, 412–427.e4 (2019).
57. E. Kheradpezhohu, M. Adibi, E. Arabzadeh, *Sci. Rep.* **7**, 11445 (2017).
58. O. Sporns, D. R. Chialvo, M. Kaiser, C. C. Hilgetag, *Trends Cogn. Sci.* **8**, 418–425 (2004).
59. I. Magrans de Abril, J. Yoshimoto, K. Doya, *Neural Netw.* **102**, 120–137 (2018).
60. P. T. Toi et al., Data for in vivo direct imaging of neuronal activity at high temporospatial resolution. Zenodo (2022); <https://doi.org/10.5281/zenodo.7114876>.

ACKNOWLEDGMENTS

We thank T.-N.-A. Dinh and G. Im for help in setting up mouse BOLD-fMRI experiments at the beginning of this study. We also thank S. Chung, J. Lee, C.-W. Woo, and S. Mangia for valuable scientific discussion; J.-K. Ryu and S. Han for pulse sequence support; C. Lee, J. W. Park, and E. Kim for MRI technical assistance; and S. Lee for administrative assistance. We acknowledge the Korea Institute of Radiological and Medical Sciences (no. 50539-2022) for providing a 9.4-T MRI facility to conduct additional experiments. **Funding:** P.T.T., S.-K.L., and J.-Y.P. acknowledge financial support from the Brain Research Program through the National Research Foundation of Korea funded by the Ministry of Science and ICT, under project ID NRF-2019M3C7A1031993. K.M. and J.L. acknowledge financial support from the same Brain Research Program, under project ID NRF-2019M3C7A1031994. H.J.J. and J.K. acknowledge financial support from the Brain Convergence Research Program through the National Research Foundation of Korea funded by the Ministry of Science and ICT, under project ID NRF-2019M3E5D2A01058328. **Author contributions:** P.T.T. and J.-Y.P. established the methodology for direct imaging of neuronal activity. P.T.T. prepared the pulse sequence and designed and conducted all animal MRI experiments. H.J.J. and J.K. designed all optogenetic experiments for MRI and electrophysiology. H.J.J. conducted the electrophysiological and optogenetic recordings and performed fluorescence and confocal imaging. H.J.J. and J.K. analyzed electrophysiological data. K.M., S.-K.L., and J.L. carried out MRI measurements of relaxation time changes in T cells and simulation. P.T.T., H.J.J., K.M., S.-P.K., S.-K.L., J.L., J.K., and J.-Y.P. contributed to data analysis and discussion. P.T.T., H.J.J., J.K., and K.M. prepared the figures and drafts. P.T.T. and J.-Y.P. wrote the paper. J.-Y.P. conceived of and supervised the project. All authors revised the manuscript. **Competing interests:** J.-Y.P. and S.-K.L. are listed as inventors on Korean patent “Methods for direct monitoring and spatial mapping of neuronal activity” (no. 10-2174092, registered on 29 October 2020). The authors declare no other competing interests. **Data and materials availability:** The data are stored and curated at Zenodo (60). **License information:** Copyright © 2022 the authors, some rights reserved; exclusive licensee American Association for the Advancement of Science. No claim to original US government works. <https://www.science.org/about/science-licenses-journal-article-reuse>

SUPPLEMENTARY MATERIALS

[science.org/doi/10.1126/science.abh4340](https://doi.org/10.1126/science.abh4340)
Materials and Methods
Supplementary Text
Figs. S1 to S26
References (61–81)
MDAR Reproducibility Checklist

[View/request a protocol for this paper from Bio-protocol.](#)

Submitted 11 March 2021; resubmitted 7 April 2022

Accepted 17 August 2022

10.1126/science.abh4340

In vivo direct imaging of neuronal activity at high temporospatial resolution

Phan Tan ToiHyun Jae JangKyeongseon MinSung-Phil KimSeung-Kyun LeeJongho LeeJeehyun KwagJang-Yeon Park

Science, 378 (6616), • DOI: 10.1126/science.abh4340

Millisecond neural activation tracking

Functional magnetic resonance imaging (fMRI) has made profound contributions to our understanding of the human brain. However, limitations in the temporal and spatial resolution of the underlying signal have prevented this technique from providing information about how cognitive functions emerge from communication between different brain regions. Toi *et al.* developed a method that allows for direct imaging of neuronal activity by fMRI (see the Perspective by van Kerkoerle and Cloos). Retaining the original benefit of high spatial resolution of MRI, the temporal resolution of this method is on the order of milliseconds. Detecting sequential propagation of neuronal activity through functionally defined networks in the brain is thus possible. The ability to image a direct correlate of neuronal spiking is a game changer for noninvasive neuroimaging. —PRS

View the article online

<https://www.science.org/doi/10.1126/science.abh4340>

Permissions

<https://www.science.org/help/reprints-and-permissions>

Use of this article is subject to the [Terms of service](#)